ISBN: 978-3-95450-233-2 ISSN: 2673-5504 doi:10.18429/JACoW-SRF2021-TUOFDV05

DYNAMICS OF RF DISSIPATION PROBED VIA HIGH-SPEED TEMPERATURE MAPPING*

R. D. Porter†, N. Banerjee, M. Liepe
Cornell Laboratory for Accelerator-Based Sciences and Education (CLASSE),
Ithaca, NY 14853, USA

Abstract

Recently, Cornell University has developed a new high-speed, high-resolution temperature mapping system that can resolve the time dynamics of RF dissipation, i.e., provide high-speed videos of the surface heating across the entire surface of the cavity. This new powerful tool allows to observe rapid changes in the local RF dissipation, as well as to resolve the dynamics of quenches, field emission processing, and other cavity events, giving new insights into these. This contribution presents the development of this new high-speed temperature mapping system, discusses its commissioning and extensive performance testing (e.g., demonstrating micro-Kelvin resolution), as well as show intriguing high-speed temperature mapping results from multiple Nb_3Sn cavities.

INTRODUCTION

Temperature mapping is a useful tool in understanding Superconducting Radiofrequency (SRF) cavity performance and limitations. This diagnostic technique involves placing numerous thermometers (often 100's) on the outside of an SRF cavity and measuring the heating of the outer cavity wall during operation. Areas of increased temperature can reveal the location of cavity quench or areas of increased resistance that lowers the cavities quality factor. These locations can then be investigated to determine what is responsible. In addition, temperature maps can reveal important information about the quench source or even identify the problem without subsequent measurements: the heat shape/distribution itself can indicate the quench culprit or heating source and heating distributions of many common problems are known [1]. Figure 1 show several examples of temperature maps and their culprits. The understanding provided helps overcome limitations in SRF cavities.

Temperature mapping of SRF cavities can be traced back to the 1980's when Cornell University developed a temperature map for 1.5 GHz cylindrical pill-box cavity [2]. Subsequently, Cornell and other institutions developed temperature maps elliptical cavities and other geometries [1, 3–5]. Temperature mapping has become a key tool in SRF and new systems continue to be developed [6, 7].

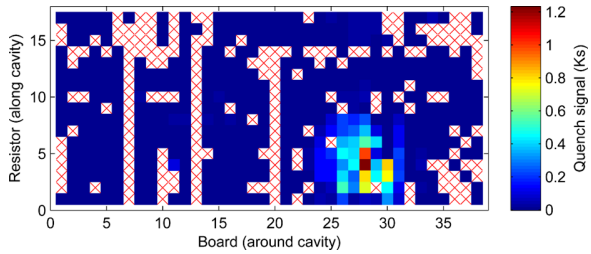

(a) A quench map of a Nb_3Sn cavity taken with the old temperature mapping system [8, 9]. The hot spot in the lower right indicates a localized thermal quench. Quench maps are acquired by allowing the cavity to quench many times and slowly measuring each sensor so that several quenches are measured on each channel. Places that are on average hotter are likely the quench site. The plot is displayed as integrated temperature. White squares with red x's indicate non-functional thermometers.

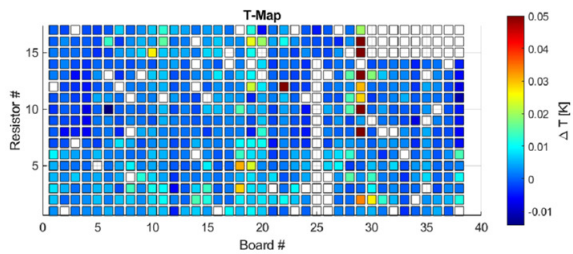

(b) A temperature map of a Nb_3Sn cavity with field emitter. The field emitter is indicated by the vertical line of heating seen in the upper right. White squares indicate non-functional thermometers.

Figure 1: Example temperature maps. These maps are read like a map of the world. The horizontal middle line is the equator of the cavity, and the top and bottom are the irises of the cavity.

Current temperature mapping systems take several minutes to read out the temperature of the entire array. This makes the systems effectively capable of only taking long exposure pictures and they cannot resolve dynamic effects. Many SRF cavity processes are dynamic: charging a cavity takes ~ 1 s, cavity quench takes place on time-scale of 0.1 – 10 ms, and D. L. Hall et. al. observed sudden, fast temperature jumps at the quench site of Nb_3Sn cavities that are speculated to be related to cavity quench [8, 9]. Measuring dynamic processes may provide important insights into the cause of quench or other performance problems in SRF cavities.

* This work was supported by U.S. DOE award DE-SC0008431 (hardware development, construction, and cavity tests.). This work was supported by the U.S. National Science Foundation under Award PHY-1549132, the Center for Bright Beams (software development, firmware development, and data analysis).
† rdp98@cornell.edu

ISBN: 978-3-95450-233-2 ISSN: 2673-5504 doi:10.18429/JACoW-SRF2021-TUOFDV05

The measurement speed of current systems are limited by their Data Acquisition (DAQ) electronics. Most of these systems rely on 1 or 2 high quality digital to Analogue to Digital Converters (ADC's) in their readout electronics. The ADC's are multiplexed to the thermometers and are read out in series. The single cell 1.3 GHz elliptical temperature map at Cornell University has 649 thermometers that must be read. Reading out these sensors one at a time is slow and sensors are not measured simultaneously, causing drifts in the helium bath temperature or slow temperature rises to distort the readout.

Recently, we have developed new DAQ electronics that has a dedicated ADC for each thermometer and can read the entire temperature map at 50 ksps. This allows for the measurement of dynamic effects and is sufficiently fast to measure the evolution of quench in SRF cavities. In addition, the new systems achieves very low noise in its measurement, as low as 15 µK depending on the mode of operation. Reading out helium bath temperature and cavity wall temperature simultaneously also allows for the correction of any helium bath temperature drifts during the measurement.

Here we discuss setup and capabilities of the system and show several examples of dynamic heating measured in Nb_3Sn cavities. Due to space limitations, details of the electronics and firmware will be limited and will be published in a subsequent paper. Discussion of Nb_3Sn measurements will focus on demonstrating the new system; scientific discussion of these measurements is discussed in another paper [10].

SYSTEM SETUP

The test system consists of a vertical test pit for testing superconducting RF cavities, temperature map, and data acquisition electronics. The overall setup of the temperature mapping system is shown in Fig. 2. Two crates of data acquisition boards sit on the warm side of the system. The DAQ boards are connected to the T-map by twisted pair ribbon cables. Cernox sensors, fluxgate magnetometers, and all standard equipment for RF testing at Cornell is also connected [9]. Additionally, the T-map DAQ boards are connected to the trigger output of Boonton 4542 RF Power Meter.

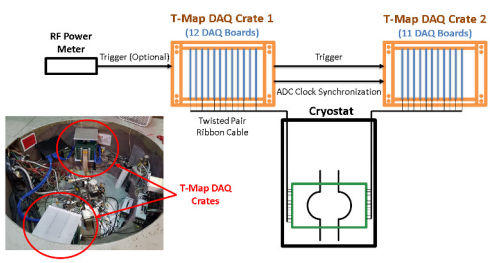

Figure 2: Diagram of experimental setup showing connection between T-map, DAQ, and power meters.

Temperature Map

To upgrade our system for high-speed/dynamic temperature mapping we only replaced the DAQ electronics. The remainder of the system has not been changed and has been detailed in previous work. Jens Knoblochs Ph.D. dissertation details the creation of a 1.5 GHz cavity T-map at Cornell and includes details on the thermometer design [1]. Subsequently, the 1.3 GHz T-map we use here was created [3]. This 1.3 GHz T-map differs only in the shape so that it fits the cavity geometry, and the removal of thermometers on the cavity beam tube. Here we provide light details on the system.

The temperature map consists of 38 printed circuit boards fitted around the cavity (see Fig. 3a). Each board holds 17 thermometers in small holders. The board is shaped so that the thermometers are pressed flat against the cavity and spaced from iris to iris (see Fig. 3b). In addition, 3 boards have a bath thermometer mounted on the side of the board that does not touch the cavity wall and measures the helium bath temperature. A small amount of thermal grease (Apiezon N-type) is applied to the thermometers and the boards are pressed against the cavity. Each thermometer is mounted on a springed pogo stick so that a. contact against the cavity wall is maintained and b. a relatively fixed and equal force is applied on all thermometers. Each thermometer is connected to the printed circuit board by manganin wires.

Due to the expense of off-the-shelf cryogenic thermometers, thermometers are made in-house. Allen-Bradley carbon resistors are used as thermometers because their resistance depends strongly on temperature at cryogenic temperatures. Typical Allen-Bradley resistors we use have a resistance change of $5 - 10\,\Omega/\mathrm{mK}$ at 2 K. These sensors come in a barrel casing. Part of the casing is filed off on the side that faces the cavity wall. This improves the sensitivity of the sensor to the cavity wall temperature. Additionally, the sensor is surrounded in a G10 housing and Stycast to provide physical support and to shield the sensor from the helium bath (see Fig. 3c).

Data Acquisition System

Temperature measurements are conducted by measuring the voltage drop over the thermometers ($\propto$ resistance). All thermometers are connected in series with a 1 MΩ resistor (within DAQ boards) and biased with a stable 6 V power supply. This creates a simple current source. The voltage is measured (details below) across the thermometer at the DAQ boards. This measurement includes additional sources of resistance, such at the twisted pair cables, but these are accounted for in the calibration. A calibration curve is made and used to convert the measured voltage to temperature (shown later).

There are 23 DAQ boards (can be scaled up) in two crates. Each DAQ board can measure 32 channels/thermometers. This gives 732 channels connected to 649 thermometers.

ISBN: 978-3-95450-233-2 ISSN: 2673-5504 doi:10.18429/JACoW-SRF2021-TUOFDV05

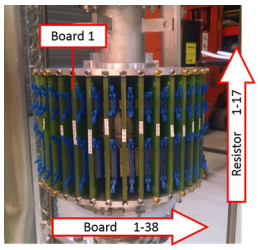

(a) Picture of the 1.3 GHz temperature map attached to a single cell cavity. Twisted pair ribbon cables have not yet been connected

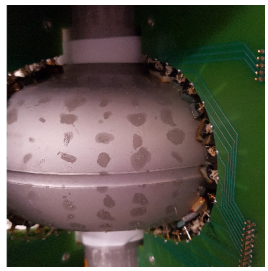

(b) Partially removed T-map boards showing location of sensors on cavity.

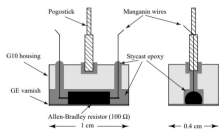

(c) Diagram of a thermometer [1]

Figure 3

Due to the pre-existing wiring, 83 channels are not connected to thermometers at the moment.

Each crate contains one leader board and 10/11 follower boards. A backplane in each crate provides power and the thermometer bias voltage to the boards and contains several interconnects (principally trigger and ADC clock synchronization). The leader board is responsible for sending a trigger signal to each board in the crate. The leader board can be triggered through ethernet, or through an external BNC connection. In addition, the leader board in Crate 1 sends a trigger signal to the leader board in Crate 2, ensuring both crates trigger simultaneously.

Each DAQ board contains a Mars ZX2 SoC module (combined FPGA and Programmable System/CPU module), 4 Analog Acquisition (daughter) Boards, ethernet connection, and additional ports for control and diagnostics. The Mars ZX2 SoC module runs embedded Linux and is responsible for accepting outside commands, configuring the system, running data acquisition, and writing data to external storage. Each analog acquisition boards collects data from 8 channels/thermometers and contains an Programable Gain Instrumentation Amplifier (PGIA), a fixed Differential Amplifier (DA) (gain = - 5), and an ADC (24-bit, 144 kHz).Voltage signals from thermometers enters the PGIA where (configurable) gain and voltage offsets are applied, it then goes through the fixed amplifier and is then digitized in the ADC.

The software and firmware architecture for the data acquisition system has three layers. The first layer consists of programable logic in the FPGA. This layer is responsible for controlling the ADCs in order to acquire data at the requested rate and store it into a fast Block RAM buffer. This buffer is small and can only hold 2048 points from each channel. It must be emptied quickly to prevent data from being overwritten. The second layer of firmware runs on the Programmable System and is responsible for moving data from the buffer to DDR3 RAM in the Mars ZX2 SoC module. Currently, the maximum data acquisition rate is set at 50 ksps and gives the programmable system sufficient time to transfer the data. The maximum acquisition time is limited by the DDR3 RAM storage to ≈ 60 s when running at 50 ksps. After data acquisition is complete the data is transferred to a network drive location via ethernet. The final level is client software written in MATLAB and running on a PC. This system transfers user commands to the DAQ boards.

An additional configuration step is run to synchronize the clocks of each individual ADC. Each ADC has an internal clock that determines when it will take its first measurement. Offsets between these clocks cause the measurements to start at slightly different times. To correct for this the leader board in crate one sends out a timing signal to all ADCs. The acquisition time windows are aligned using a special aperture trigger. This aligns the ADC clock to sample at the same time. After this is done the maximum offset between triggers is 20 ns, which is determined by the distance the signals have to travel. The offset is much less than the minimum sample time of 20 µs [11].

DATA ACQUISITION PROCESS

Here we detail the data acquisition process we are using for the T-map. It consists of three main parts: calibration, RF-off measurement, and RF-on measurements. In addition, we discuss some of the typical data post processing. This information is needed both to understand the T-map results, and to understand noise analysis in the next section. In addition to T-map measurements, we measure the quality factor vs field and temperature for the cavity.

To convert voltage to temperature a calibration curve must be made for each thermometer. The calibration is created by measuring both the T-map (25,000 points each in 1 s) and a calibrated Cernox sensor (at the cavity equator) from 4.2 K (in liquid helium) down to just below the lowest measurement temperature without applying RF to the cavity (at the time of measurement). As long as the cooldown rate is slow enough there should not be a significant temperature gradient from the top of the T-map to the bottom. These measurements are taken roughly every 0.05 K during the cooldown. The resulting curve is fit to a modified regression model of a semimetal: $V(T) = V_0 - V_\infty e^{\frac{S}{T}}$ [11–13]. An example calibration curve and fit is shown in Fig. 4. The resistance of these thermometers changes significantly when thermal cycled to room temperature, and they must be calibrated every time the T-map is used.

At desired measurement temperatures two 20 s T-map measurements are taken with the RF power off (RF-off). This serves two purposes. The difference of the two RF-off temperature maps is used to find broken channels: the differ-

ISBN: 978-3-95450-233-2 ISSN: 2673-5504 doi:10.18429/JACoW-SRF2021-TUOFDV05

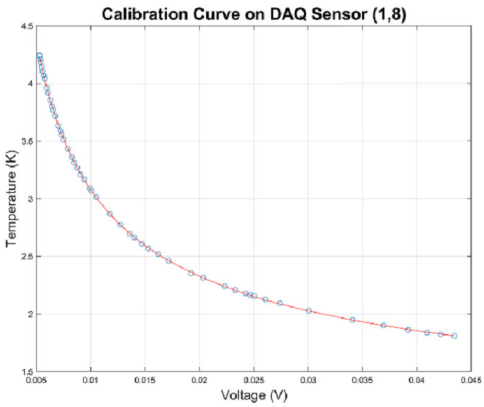

Figure 4: Example calibration data for the temperature map. Fit model shown in red.

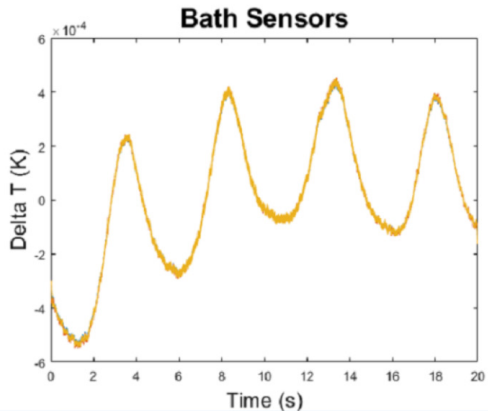

Figure 5: Temperature of 3 bath sensors during an T-map acquisition at 1.8 K. Some smoothing applied and mean values subtracted. Note the 300 µK oscillations caused by the cryogenics system.

ence should have a mean close to zero, and some statistical noise (when analyzing time data) on each channel. Channels that lie outside of normal bounds are determined to be faulty. In addition, the RF-off measurements reveal the offset between a T-map sensor and a bath sensor, so the offset can be corrected.

RF-on T-maps are taken with the power on. These can be one of two forms: static or dynamic. For static T-maps the cavity is charged, allowed to reach equilibrium, and short T-map is taken. This is the equivalent of older T-maps, but our new system can achieve much better temperature resolution (down to 15 µK at 1.8 K). For the dynamic T-maps shown here, the T-map is configured for a long measurement (e.g. 20 s) at 25 ksps or 50 ksps) and to trigger off the RF power meter; the RF power meters are configured to tirgger off a rise in measure forward power; and the power is turned on causing the power meters and T-map to trigger simultaneously and both the RF power and temperature is recorded.

The final temperature map data is calculated as a difference in temperature, ΔT, between the T-map temperature and the bath thermometer. An additional correction is applied of the difference between T-map thermometer and the bath thermometer during an RF-off measurement. This helps remove any offsets from the calibration. Figure 5 demonstrates the importance of correcting for the bath temperature. The helium bath is warming because of heating during the measurement, and there is a 300 µK oscillation in the temperature. This oscillation is caused by a control loop opening and closing a valve to try to keep the temperature in the test Dewar constant.

$$\Delta T\left(i,j,t\right) = T_{ON}\left(i,j,t\right) - T_{BATH,ON} - \overline{\left(T_{OFF}\left(i,j\right) - T_{BATH,OFF}\right)} \quad (1)$$

NOISE AND UNCERTAINTY ANALYSIS

An important figure of merit of a temperature mapping system is the measurement uncertainty. If we want to measure low heat phenomena (low field resistance, etc.) we need low uncertainties, and some dynamic effects may result in only small changes. There are three main uncertainties in the system that we will consider: measurement noise, calibration uncertainties, and sensor sensitivity to cavity wall temperature. Overall the noise is low compared to our previous system.

After correction for bath temperature oscillations there are two main sources of nosie [11]: 60 Hz noise from outside sources, and noise from the PGIA amplifier and offset. 60 Hz is fairly small in the system and can easily be filtered in the frequency domain if needed. A breakdown of noise from the electronic components is shown in Fig. 6. Noise from the PGIA is the most significant source. Since these electronics are on the warm side, the operation temperature makes no difference in the overall noise. The PGIA noise depends on frequency and increases as the sample rate does. In current configuration of the T-map the standard deviation of the noise is ≈ 30 µK at 1 ksps, increasing to ≈ 150 µK at 50 ksps.

The calibration curve provides another source of error. We have computed standard deviation estimates of our fit values and temperature readings [11]. An example for one thermometer is shown in Fig. 7 and is fairly representative of all thermometers. The standard deviation varies with temperature and is ≈ 15 µK at 2 K.

Figure 8 show standard deviation and mean values for all thermometers when two RF-off measurements (at the same bath temperature) are used in Eq. 1. Ideally, the resulting value would be zero. This gives us an idea of the statistical (mean of standard deviation) and systematic (standard deviation of mean) noise in the system, 154 µK and 14 µK respectively at 1.9 K.

These two measures of uncertainty demonstrate a great improvement in our temperature mapping system. Our old system, when averaging over several measurements could only achieve an uncertainty of ≈ 1 mK. With the lower noise

ISBN: 978-3-95450-233-2 ISSN: 2673-5504 doi:10.18429/JACoW-SRF2021-TUOFDV05

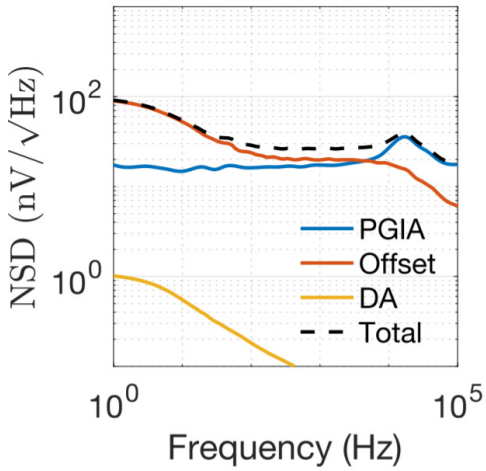

Figure 6: Modeled noise contributions of electronic components of the T-map DAQ electronics [11]. The noise is dominated by contributions from the amplifiers. Noise from other components, such as the ADC, are negligible.

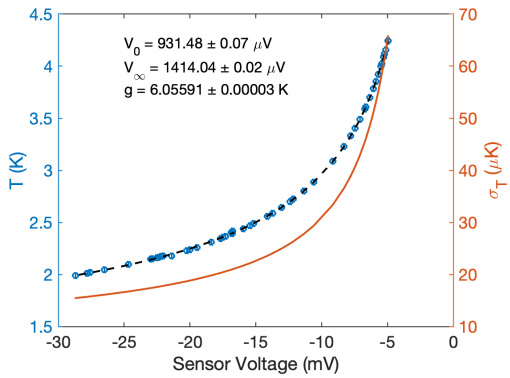

Figure 7: Calibration curve and uncertainty of calibration of a T-map thermometer [11].

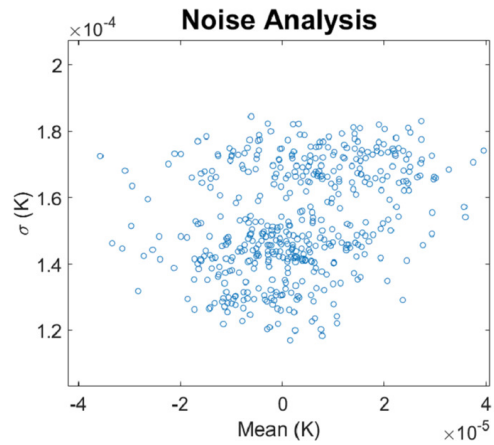

Figure 8: A scatter plot of the mean and standard deviation of each thermometers in the T-map at 1.8 K. This is showing the bath temperature corrected difference between two RF-off T-maps, each 1,000,000 points taken at 50 ksps. The mean standard deviation and standard deviation of the mean provide an estimate of the statistical and systematic noise in the system.

electronics and bath oscillation correction we can get the uncertainty down to ≈ 15 μK after averaging.

There is one more source of uncertainty to consider: sensor sensitivity to cavity wall temperature. When measuring the cavity wall temperature the thermometer is both being warmed by the cavity wall and cooled by the liquid helium bath. The final temperature of the sensor is somewhere between the wall temperature and the helium bath temperature. We refer to the fraction of the thermometer temperature rise to the real wall temperature rise as the sensitivity. A previous estimate from Cornell found that the sensitivity of one of our sensors is 0.35 ± 0.13 [14]. This suggests an additional 37% uncertainty in all temperature rise measurements. In addition, many aspects may affect this estimate: quantity and consistency of thermal paste used, Kapitza resistance of cavity wall, and operating temperature could conceivably change the value. This additional systematic uncertainty in the temperature increase is only relevent for certain measurements.

The cavities measured here have a large indent at the equator weld seam that creates poor thermal contact at the equator. This reduces the sensitivity of the sensors at the weld seam. In all the results we show here our equator has zero heating on the scale displayed. In some cases, this is likely because of the poor contact made by equator sensors.

DYNAMIC MEASUREMENTS

Now we will present several examples of dynamic temperature map measurements made on Nb_3Sn cavities. Nb_3Sn is an promising area of SRF research. The cavities are comprised of 3 μm of Nb_3Sn on niobium bulk. The material achieves high quality factors ($\approx 2 \cdot 10^{10}$) at 4.2 K and could theoretically achieve accelerating gradients of 100 MV/m in TESLA elliptical cavities [9, 15–19]. However, Nb_3Sn cavities are currently limited to 17 – 24 MV/m. The cause of cavity quench is an area of ongoing research [9, 20, 21]. Temperature mapping has been used to identify a quench site, but subsequent optical and electron microscopy inspection has not revealed an obvious culprit [9]. This makes Nb_3Sn an exciting candidate for dynamic temperature mapping: any additional information could help in determining the quench mechanism.

Cavity Charge and Discharge

Figure 9a shows the average temperature of the temperature map while the cavity is charged and discharged at 1.8 K. The temperature follows the transmitted power/energy curve of the cavity except for a slow rise in temperature during operation. The forward, reflected, and transmitted power were recorded, and the external quality factor was determined from quality factor measurements. Combining these we can calculate the quality factor as a function of time as the cavity is charged and discharged (see Fig. 9b). Similarly, we can calculate the quality factor from the temperature/heating and the transmitted power up to an unknown constant (depending on sensor sensitivity, Kapitza resistance, and other thermal

ISBN: 978-3-95450-233-2 ISSN: 2673-5504 doi:10.18429/JACoW-SRF2021-TUOFDV05

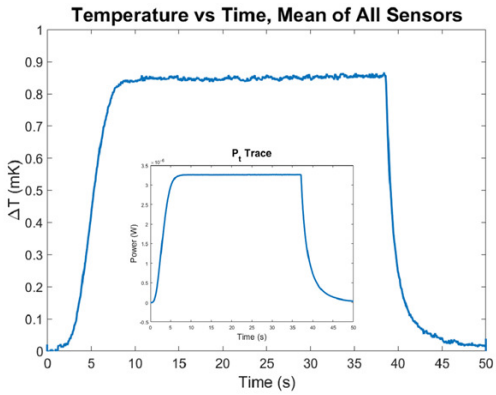

(a) Average temperature of all functioning sensors on T-map during a charge-discharge cycle of the cavity. Some smoothing applied. Inner plot displays the transmitted power with is proportional to the energy in the cavity. Measurement were done at 1.8 K.

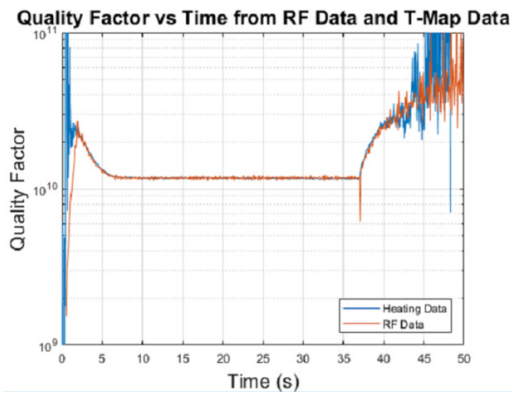

(b) The quality factor vs time during the RF power charge-discharge cycle. The quality factor is calculated from recorded RF power data, and again from the wall temperature and transmitted power from the cavity.

Figure 9

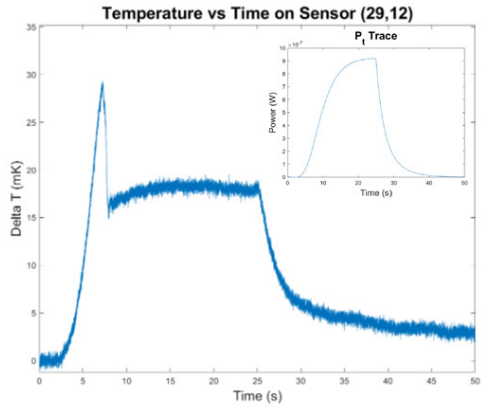

Figure 10: The temperature of a T-map thermometer during a charge-discharge cycle of the cavity. Some smoothing applied. Inner plot displays the transmitted power with is proportional to the energy in the cavity. Measurement done at 4.2 K. Notice that the temperature rises and then suddenly drops.

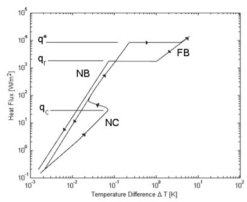

(a) Schematic of regions of different steady-state heat flow behavoirs vesus the heat flow plot. The y-axis shows the elevated temperature of the wall compared to the helium bath. Figure taken from [22].

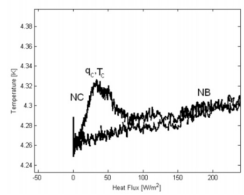

(b) Temperature of a heated wire in liquid helium demonstrating the transition from normal convection to nucleate film boiling regime. Figure taken from [22].

Figure 11

properties of the cavity). We scale the quality factors to match at one location and see very good agreement across the rest of the curve.

Temperature Slips

At 4.2 K (or anywhere above the superfluid transition temperature) we see interesting dynamics in the charge-discharge cycles. Figure 10 shows the temperature on one thermometer. The temperature rises and then suddenly falls/slips. This slip appears on every thermometer on the T-map (when above the superfluid transition temperature), but do not occur at the same time, surface field, or local temperature: there is some amount of randomness.

This is likely a transition from convection cooling to nucleate film boiling at the liquid helium-Nb_3Sn interface [22]. Figure 11a shows a diagram of different steady-state heat flow regimes. The low heat flux mode is convection cooling. At slightly higher heat fluxes the system can transition to nucleate film boiling. This substantially improves the interface conductance, cooling the cavity wall and resulting in a temperature drop. Much of the conduction cooling area is meta-stable, explaining the somewhat random timing of the temperature drop. Experiments heating metal wires in liquid helium baths show almost identical temperature curves (see Fig. 11b) [22].

Temperature Jumps

Temperature jumps were previously observed at the quench site of Nb_3Sn cavities [8, 9]. These can be seen in Fig. 12a. As the cavity charges we first see Ohmic heating, as expected, but then the temperature suddenly jumps up. When the cavity discharges there are jumps back down, but there is a hysteresis. The cavity does not quench during the cycle. There has been much speculation as to the cause of the these jumps and how they might be related to quench [9, 21].

These jumps were measured using a single ADC to study dynamic heating at only the quench site. They are fundamentally a dynamic effect. Now that we have a high-speed T-map

ISBN: 978-3-95450-233-2 ISSN: 2673-5504 doi:10.18429/JACoW-SRF2021-TUOFDV05

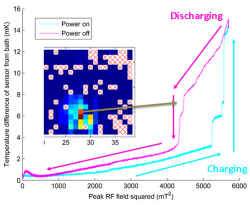

(a) Temperature vs surface magnetic field at the quench site of an Nb_3Sn cavity as the cavity is charged and discharged [9]. Notice the sudden jumps in temperature even though the cavity does not quench.

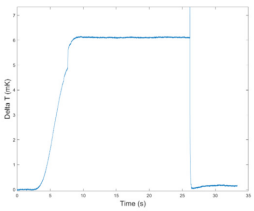

(b) One of many channels where a jump in temperature is observed (at $\approx$ 8 s) while the cavity is charging. Another small jump is seen while charging. This cavity quenches at $\approx$ 26 s.

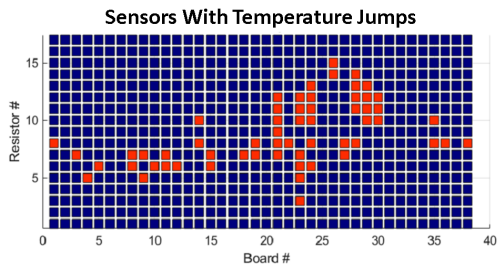

(c) All channels where a temperature jump was observed are marked in red.

Figure 12

that can measure every thermometer at once it is interesting to see if we see these jumps again.

Figure 12b shows jumps observed on one T-map thermometer using our dynamic T-map. Jumps of various heights were observed on many T-map thermometers: 59 thermometers in total (see Fig. 12c). This dynamic effect is far more widespread than previously realized. Further study will hopefully reveal something about Nb_3Sn performance.

Quench Video

Figure 13 shows a frame from the first quench of this cavity after it was cooled to 1.8 K. Unfortunately, papers do a poor job of displaying videos. The quench takes place over $\approx$ 50 ms and at 17 MV/m. Quench is occurring along the equator on the right side of the T-map. The quench is not localized but spread along the T-map. It did not originate in one spot and spread but turned on across the entire region. This is likely a multipacting quench being recorded.

This was not expected based on previous measurements. Figure 1a shows a quench map of a previously measured Nb_3Sn cavity. The quench region is highly localized and not at the equator. It is fundamentally different than the multipacting we observe now.

Quench Site Evolution

We can record the temperature as the cavity continues to quench and we see evolution of the quench site. Figure 14 shows a T-map over the next 32 cavity quenches and time

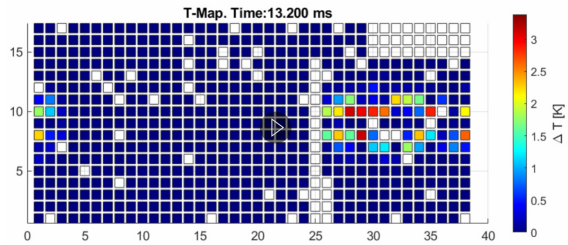

Figure 13: A frame from a quench T-map video. This shows what appaers to be a multipacting quench.

resolved temperature at the two hotspots. We can see that there are now two quench regions: along the equator, and at a localized spot (as was seen in historic quench maps of Nb_3Sn cavities). The quenches move back and forth between the two sites (with some movement on the equator as well). The quenches settled on the second, localized site. The next 100 quenches were recorded and all of them were on the second site. A possible explanation is that we processed the multipacting site and hit a defect at almost the exact same field, but more study is required.

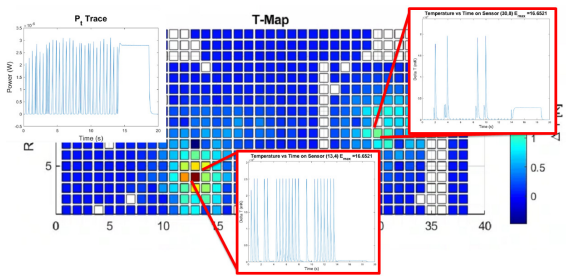

Figure 14: A temperature map showing the average temperature while the cavity is quenched 32 times. Two different hot spots emerge, indicating two quench locations. Two temperature vs time plots are overlayed for a thermometer in each quench region. Large temperature spikes indicate quench at or near the thermometer. Medium height temperature spikes indicate a quench that is still somewhat near (still on the equator). We can see that quench is moving between the equator and the hot spot in the lower left.

We could not see the first multipacting quench with the old system because taking a quench map required quenching the cavity 100's of times. Since this quench site moves after only one quench we could never see it with the old system.

CONCLUSION

We have built a high-speed temperature mapping system that can acquire data at 50 ksps. This provides sufficient speed to measure quench and other thermal dynamics. In our commissioning tests we measured multiple dynamic heating phenomena: temperature jumps, cavity quench, and evolution of a quench site. This demonstrates both the capabilities of the system and that there are important dynamics that have never been measured.

ISBN: 978-3-95450-233-2 ISSN: 2673-5504 doi:10.18429/JACoW-SRF2021-TUOFDV05

In addition, the new system attains very low noise: down to 15 µK. This allows for very sensitive temperature measurements. This opens new possibilities to measure low heating phenomena such as resistance at low accelerating gradients or taking temperature maps near the critical temperature.

The tool is already providing new insights into Nb_3Sn dynamics. We have shown widespread temperature jumps, and new quench dynamics that could not be measured with older temperature maps. Overall, high-speed temperature mapping provides a new window into SRF science and performance.

REFERENCES

[1] J. Knobloch, "Advanced Thermometry Studies of Superconducting Radio-Frequency Cavities," Ph.D. dissertation, Phys. Dept., Cornell University, Ithaca, NY, USA, 1997.

[2] K. Kneisel, G. Mueller, and C. Reece, "Investigation of the Surface Resistivity of Superconducting Niobium Using Thermometry in Superfluid Helium," in *Proc. Applied Superconductivity Conf.*, Baltimore, MD, USA, 1986.

[3] S. Posen *et al.*, "Residual Resistance Studies at Cornell," in *Proc. IPAC'12*, New Orleans, LA, USA, Jul. 2012, paper WEPPC079.

[4] Q. S. Shu *et al.*, "An Advanced Rotating T-R Mapping and It's Diagnoses of TESLA 9-Cell Superconducting Cavity," presented at PAC'95, Dalas, TX, USA, May 1995, paper TPP11.

[5] A. Canabal *et al.*, "Development of a Temperature Mapping System for 1.3-GHz 9-Cell SRF Cavities," presented at PAC'07, Albuquerque, NM, USA, Jun. 2007 paper WEPMS031.

[6] Z. A. Conway, D. L. Hartill, H. S. Padamsee, and E. N. Smith, "Defect Location in Superconducting Cavities Cooled with He-II Using Oscillating Superleak Transducers," in *Proc. SRF'09*, Berlin, Germany, Sep. 2009, paper TUOAAU05.

[7] J. Köszegi, B. Schmitz, K. Alomari, O. Kugeler, and J. Knobloch, "A Combined Temperature and Magnetic Field Mapping System for SRF Cavities," in *Proc. IPAC'18*, Vancouver, BC, Canada, Apr. 2018, paper TUZGBE5.

[8] D. L. Hall *et al.*, "Cavity Quench Studies in Nb3Sn Using Temperature Mapping and Surface Analysis of Cavity Cutouts," in *Proc. SRF'17*, Lanzhou, China, Jul. 2017, paper THPB041.

[9] D. L. Hall, "New Insights into the Limitations on the Efficiency and Achievable Gradients in Nb3Sn SRF Cavities," Ph.D. dissertation, Phys. Dept., Cornell University, Ithaca, NY, USA, 2017.

[10] R. D. Porter, N. Banerjee, and M. Liepe "Dynamic Temperature Mapping of Nb3Sn Cavities," presented at SRF'21, East Lansing, MI, USA, Jun. 2021, paper SUPCAV003, this conference.

[11] N. Banerjee, "Towards More Efficient Accelerating RF Systems: Superconducting Energy Recovery LINACs and Thermometry of High Q Cavities," Ph.D. dissertation, Phys. Dept., Cornell University, Ithaca, NY, USA, 2020.

[12] S. Rudtsch and C. Rohden, "Calibration and Self-Validation of Thermistors for High-Precision Temperature Measurements," *Measurement*, vol. 76, p. 1, Dec. 2015. doi:10.1016/j.measurement.2015.07.028

[13] J. S. Steinhart and S. R. Hart, "Calibration Curves for Thermistors," *Deep Sea Research and Oceanographic Abstracts*, vol. 15 n. 4, p. 497, Aug. 1968. doi:10.1016/0011-7471(68)90057-0

[14] G. Mueller and P. Kneisel, "Development of sensitive thermometers for calibrated surface temperature measurements of niobium cavities immersed in superfluid helium," Cornell University, Laboratory of Nuclear Studies, Ithaca, NY, USA, Rep. SRF report 851291 EX, 1985.

[15] S. Posen and M. Liepe, "Advances in development of Nb3Sn superconducting radio-frequency cavities," *Phys. Rev. ST Accel. Beams*, vol. 17, p. 112001, Nov. 2014. doi:10.1103/PhysRevSTAB.17.112001

[16] S. Posen and D. L. Hall, "Nb3Sn Supercondcution Radiofrequency Cavities: Fabrication, Results, Properties, and Prospects," *Superconductor Science and Technology*, vol. 30, no. 3, p. 33004, Jan. 2017. doi:10.1088/1361-6668/30/3/033004

[17] S. Posen, "Understanding and Overcoming Limitation Mechanisms in Nb3Sn Superconducting RF Cavities," Ph.D. dissertation, Phys. Dept., Cornell University, Ithaca, NY, USA, 2014.

[18] A. Godeke, "A review of the properties of Nb3Sn and their variation with A15 composition, morphology and strain state," *Superconductor Science and Technology*, vol. 19, no. 8, p. R68, Aug. 2006. doi:10.1088/0953-2048/19/8/r02

[19] G. Cetelani and J. P. Sethna, "Temperature Dependence of the Superheating Field for Superconductors in the high-kappa London Limit," *Phys. Rev. B*, vol. 78, no. 22, p. 224509, Dec. 2008. doi:10.1103/PhysRevB.78.224509

[20] D. Porter *et al.*, "Field Limitation in Nb3Sn Cavities," presented at SRF'19, Dresden, Germany, Jul. 2019, paper THFUA5, unpublished.

[21] R. D. Porter *et al.*, "Progress in Nb3Sn SRF Cavities at Cornell University," in *Proc. NAPAC'19*, Lansing, MI, USA, Sep. 2019, paper MOYBB3.

[22] J. Lantz, "Heat Transfer Correlations Between a Heated Surface and Liquid and Superfluid Helium," M.Sc. thesis, Engineering and Management Dept., Linkopings Universitet, Linkoping, Sweden, 2007.